

See discussions, stats, and author profiles for this publication at:
<https://www.researchgate.net/publication/255218591>

Nature of the parasitic chemistry during AlGaInN OMVPE

ARTICLE *in* JOURNAL OF CRYSTAL GROWTH · JANUARY 2003

Impact Factor: 1.7 · DOI: 10.1016/j.jcrysgro.2003.11.074

CITATIONS

71

READS

52

4 AUTHORS, INCLUDING:



George T Wang

Sandia National Laboratories

119 PUBLICATIONS 1,857 CITATIONS

SEE PROFILE



Michael E. Coltrin

Sandia National Laboratories

135 PUBLICATIONS 4,264 CITATIONS

SEE PROFILE



J. Randall Creighton

Sandia National Laboratories

71 PUBLICATIONS 1,788 CITATIONS

SEE PROFILE

Nature of the parasitic chemistry during AlGaInN OMVPE

J. Randall Creighton*, George T. Wang, William G. Breiland, Michael E. Coltrin

Sandia National Laboratories, P.O. Box 5800, MS-0601, Albuquerque, NM 87185, USA

Abstract

Using in situ laser light scattering, we have observed gas-phase nanoparticles formed during AlN, GaN and InN OMVPE. The response of the scattering intensity to a wide range of conditions indicates that the AlN parasitic chemistry is considerably different from the corresponding GaN and InN chemistry. A simple CVD particle-growth mechanism is introduced that can qualitatively explain the observed particle size and yields a strong residence time dependence. We also used FTIR to directly examine the reactivity of the metalorganic precursors with NH_3 in the 25–300°C range. For trimethylaluminum/ NH_3 mixtures a facile CH_4 elimination reaction is observed, which also produces gas-phase aminodimethylalane, i.e. $\text{Al}(\text{CH}_3)_2\text{NH}_2$. For trimethylgallium and trimethylindium the dominant reaction is reversible adduct formation. All of the results indicate that the AlN particle-nucleation mechanism is predominately of a concerted nature, while the GaN and InN particle-nucleation mechanisms involve homogeneous pyrolysis and radical chemistry.

© 2003 Elsevier B.V. All rights reserved.

Keywords: A1. Fourier transform infrared spectroscopy; A1. Laser light scattering; A3. Metalorganic vapor phase epitaxy; A3. Organometallic vapor phase epitaxy; B1. Aluminum nitride; B1. Gallium nitride; B1. Indium nitride

1. Introduction

Organometallic vapor phase epitaxy (OMVPE) is a highly successful method of depositing AlGaInN material, but unfortunately it is often complicated by parasitic gas-phase chemical reactions [1–6]. One consequence of the parasitic reactions is that the growth rate and/or film incorporation efficiency become very temperature dependent at conditions where they otherwise would be nearly temperature independent (i.e. during mass transport limited growth). The growth rate (or incorporation efficiency) is also

no longer a linear function of the input group-III concentration. The temperature dependence and the nonlinear concentration dependence make it much more difficult to control alloy composition. It is generally believed that reactions between ammonia and trimethylgallium (TMGa), or trimethylaluminum (TMAI), or trimethylindium (TMIn), are responsible for effectively removing group-III material from the deposition process. However, the mechanistic details of the reaction chemistry are still poorly understood. We have recently demonstrated that gas-phase nanoparticles are formed during AlN, GaN, and AlGaIn OMVPE [6,7]. These nanoparticles represent the end product of a chain of gas-phase chemical reactions. Thermophoresis keeps the nanoparticles from reaching the surface, so the mass tied up in

*Corresponding author. Tel.: +1-505-844-3955; fax: +1-505-844-3211.

E-mail address: jrcreig@sandia.gov (J.R. Creighton).

them represents a deleterious loss of material from the gas stream.

From a variety of observations, including the residence time dependence for GaN and AlN growth rates [6], we have proposed that nanoparticles grow considerably in size by a CVD-type mechanism (see Fig. 1, right-hand side). The CVD particle-growth mechanism may, or may not involve the same type of chemistry involved in the particle-nucleation mechanism. In this paper we review some of our previous results for AlN- and GaN-derived nanoparticles, report new observations for InN OMVPE, and discuss many of the trends and implications. We also introduce a simple particle-growth rate expression that can explain several observations.

The particle-nucleation mechanism may involve two classes of chemical reactions, which are shown schematically in Fig. 1. The lower pathway (a) begins with adduct formation and is followed by a concerted CH_4 elimination step forming a $(\text{CH}_3)_2\text{MNH}_2$ species (sometimes referred to as an “amide” [8]), e.g. $(\text{CH}_3)_2\text{AlNH}_2$ (aminodimethylalane). In the solid phase the Al and Ga version of this molecule exists as a trimer, e.g. $[(\text{CH}_3)_2\text{AlNH}_2]_3$ [9,10], and there is some evidence for association in the gas-phase [10,11]. Further CH_4 elimination and association (oligomerization) may occur, eventually leading to clusters (or

nuclei) large enough to support growth by a CVD process. One aspect of the concerted path-A is that it involves reactions with relatively low activation energy (<40 kcal/mol) [12–15]. Miho-polous et al. [12] used a mechanism of this type, with thermophoresis considerations, to explain many AlN OMVPE observations. Due to the concerted nature of this pathway the carrier gas has little way to directly participate in the chemistry.

It is sometimes proposed that the adduct or amide-trimer could be directly responsible for the parasitic chemical effects, but the small reduction in diffusivity of these molecules (compared to the precursor) cannot account for the observed diminution in growth rate. Reduced surface reactivity of these molecules seems unlikely, given the high temperatures involved. The fact that several of these molecules have been used as growth precursors also implies sufficient reactivity. If the adduct vapor pressure is exceeded condensation may occur [16], but this process cannot explain the majority of the observed parasitic behavior.

A second reaction pathway, Fig. 1(b) or path-B, is initiated by homogeneous pyrolysis of the metalorganic precursor into radical fragments. Further loss of CH_3 radicals may occur, and the metal-containing fragments may recombine into clusters or nuclei large enough to sustain a CVD-growth mechanism. This pathway involves reactions with higher activation energies (>40 kcal/mol), and therefore requires high temperatures before it becomes viable. As an example, the first step for TMGa pyrolysis; $\text{TMGa} \rightarrow \text{DMGa} + \text{CH}_3$, has an activation energy of at least 60 kcal/mol [17,18]. Since path-B involves radical reactions, it is more likely that the carrier gas might directly influence the chemistry. For instance, the pyrolysis rate of both TMGa and TMIIn are accelerated in H_2 relative to the rate in inert gases [19,20].

We have used Fourier transform infrared spectroscopy (FTIR) to examine the initial reactivity of gas-phase ammonia with TMAI, TMGa, and TMIIn, from room temperature up to $\sim 300^\circ\text{C}$. Results of this study shed some light on the type of reaction pathway available for each

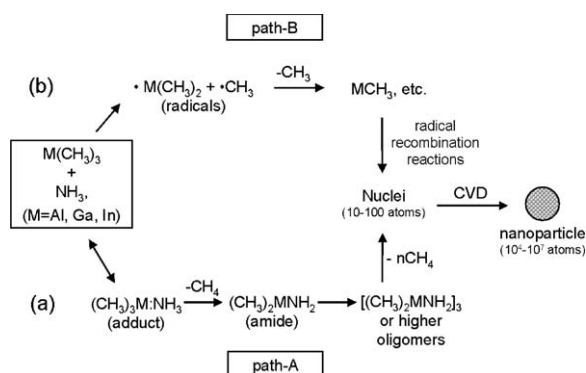


Fig. 1. Schematic of two Group-III nitride OMVPE parasitic chemical pathways that lead to nanoparticle nucleation. (a) Adduct formation followed by concerted chemical reactions (low activation energies) that evolve CH_4 . (b) Bond homolysis reactions (high activation energies) evolving CH_3 radicals, followed by radical recombination.

precursor, and are reported in the second half of this paper.

2. Experimental procedure

Light scattering experiments were performed in an inverted stagnation point flow reactor constructed of standard vacuum components, which has been described elsewhere [7]. Briefly, a GaN-coated resistively heated molybdenum disk (2.54-cm dia) served as the substrate. This reactor is installed in parallel with our research rotating disk reactor (RDR) and utilizes the same gas-handling system. Operating conditions for the inverted flow reactor are similar to our RDR OMVPE conditions, although the total flow rates have been reduced by a factor of ~ 2 to account for the decreased tube diameter of the inverted flow reactor. An Ar^+ ion laser was used as the light source (50 mW, $\lambda = 488$ nm), with the beam expanded into a sheet approximately 2 cm wide. The beam enters the reactor through a window and passes just below the surface of the heater. Light scattering is observed near 90 degrees from the laser direction. For quantitative scattering intensity measurements, images were collected with a CCD camera.

Gas-phase infrared spectroscopy was performed with a Mattson RS-1 FTIR. A custom long pathlength cell that could be heated to 300°C was mounted in the sample compartment of the instrument. The gas cell has a pathlength of 80-cm, and an internal volume of 3.2 l, more details will be reported elsewhere [21]. The gas cell was also connected in parallel with our research RDR, and operated at flow rates and pressures in the same nominal range used for AlGaInN OMPVE. Gases were mixed before injection into the cell, with concentrations kept below the onset of adduct condensation [16]. The total pressure was varied over 50–300 torr, with a typical total flow rate of 6.5 slm. For this flow rate, at 300 K and 100 Torr total pressure, the mean residence time of the gases in the cell is 3.5 s. For most experiments hydrogen was used as the carrier gas. A methane line was added for calibration purposes. At room temperature, 100 Torr total pressure and 6.5 slm total flow,

the detection limit for CH_4 corresponds to a flow rate of $\sim 1 \mu\text{mol/min}$. The temperature was measured at several points internally, and the uniformity was $< 5^\circ\text{C}$.

Spectra were collected with a 2 cm^{-1} resolution, typically from $450\text{--}4000 \text{ cm}^{-1}$. At the higher cell temperatures the increased absorption by the KCl window limited the lower effective wavenumber to $\sim 500 \text{ cm}^{-1}$. For conditions with both metalorganic precursor and NH_3 flowing through the cell, a corresponding reference spectrum was recorded with NH_3 only. Because of the very strong NH_3 IR absorption, small concentration differences between the sample and reference spectra, and/or slight inaccuracies in the data acquisition often led to small residual NH_3 -derived features on the baseline. These small artifacts are sometimes noticeable in the data reported, particularly at 3335 , 1626 , 964 , and 930 cm^{-1} , which are the strongest peaks in the NH_3 IR spectrum.

3. Light scattering observation of gas-phase nanoparticles

We have used in situ laser light scattering to make experimental observations of gas-phase nanoparticles formed during AlN, GaN and recently InN OMVPE. A typical result for GaN is shown in Fig. 2(a). Reactor conditions are:

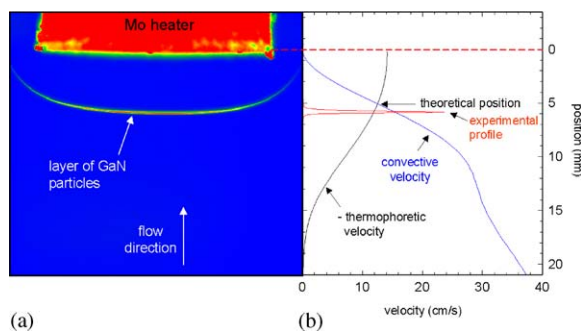


Fig. 2. (a) GaN-derived particles observed near standard OMVPE conditions (false color image. A similar band of particles was seen for AlN and InN. (b) Experimental scattering profile along the centerline of the reactor, with peak position at 5.8 ± 0.2 mm. Thermophoretic and convective velocities sum to zero at 5.1 mm.

surface temperature = 983°C, total pressure = 140 Torr, H₂ flow = 5.5 slm, NH₃ flow = 1.0 slm, TMGa flow = 182 μmol/min. For these conditions particles are easily observed with the naked eye. Similar results are obtained for AlN, InN, and mixtures thereof. The particle profile is flattened near the center of the heater, but the particles appear to follow a streamline up and around the disk. Along the centerline of the reactor, the band of particles is located 5.8 ± 0.2 mm upstream from (below) the surface, see Fig. 2(b). These particles are formed by chemical reactions that require the high temperatures encountered in the boundary layer. Thermophoresis keeps the particles from reaching the surface so they can not contribute to the deposition rate, and the balance of thermophoretic and viscous forces defines their position. The particle position shifts slightly as the surface temperature, and therefore temperature gradient, is varied. The fluid dynamics of this reactor were modeled using the MPSalsa code [22], which allows us to determine the expected particle position [7]. The thermophoretic and convective velocities sum to zero at 5.1 mm (see Fig. 2(b)), which is in reasonable agreement with the experimental observation of 5.8 ± 0.2 mm.

We note that the particles are well within the thermal boundary layer. For a substrate temperature near 1000°C, the particles reside at temperatures of 600–700°C, which is sufficient to drive a variety of chemical reactions, including heterogeneous chemistry on the particle surfaces. Therefore, it is possible that once particles have nucleated they may grow considerably in size by a chemical vapor deposition (CVD) process. The growth kinetics of small spherical particles has been described previously [23], and the steady state radial growth rate (dr/dt) is given by Eq. (1), where ρ is the particle atomic density, D the diffusivity, C° the input concentration, s the reactive sticking coefficient, v the mean molecular velocity. This simple analysis ignores possible reactant depletion effects. In the small size limit; $r \ll 4D/(s \cdot v)$, the rate reduces to Eq. (2), which is simply the kinetic limit defined by the product of the collision rate and reactive sticking coefficient. At our normal working pressure of 140 Torr, $4D/(s \cdot v)$ is on the order of 10^4 nm

(assuming $s \sim 1$).

$$\rho \cdot dr/dt = D \cdot C^\circ / [r + 4D/(s \cdot v)] \quad (1)$$

$$\rho \cdot dr/dt \approx \frac{1}{4} s \cdot v \cdot C^\circ \quad \text{when } r \ll 4D/(s \cdot v). \quad (2)$$

The radial growth rate from Eq. (2) can be as high as $\sim 10^3$ nm/s for typical GaN and AlN OMVPE conditions (again, assuming $s \sim 1$). It is interesting to note that this growth rate is $\sim \times 10^4$ higher than the diffusion-limited growth rate for planar (1D) films. Using a nominal boundary layer residence time of ~ 0.1 s implies that particles may grow as large as ~ 200 nm in diameter by this mechanism. By measuring the angular dependence of light scattering intensity we found that AlN particles were 35–50 nm in diameter [7]. Using a thermophoretic particle capture technique [24] and TEM analysis, we have found that AlN, GaN, and InN OMVPE produces an abundance of gas-phase nanoparticles in the 5–50 nm range [25]. Therefore, the particle CVD growth mechanism is easily capable of generating the size range observed experimentally.

An important consequence of the particle CVD growth mechanism is that because the radius grows linearly in time, the volume (and therefore mass) of the particles increases as fast as τ^3 (τ = residence time). A high-order dependence on τ may be the source of the high-order spin rate (Ω) dependence we observed for GaN and Al growth rates in our RDR, i.e. growth rate $\propto \Omega^{1.5-2.5}$ [6]. The connection is because the boundary layer residence time and Ω are interrelated, $\tau \propto 1/\Omega$ for an ideal rotating disk reactor [26]. The particle-growth mechanism provides an effective autocatalytic pathway for the parasitic chemical process, which is difficult to achieve with simple unimolecular or bimolecular reaction channels.

Many of the trends observed for the scattering intensity from GaN, AlN, and InN-derived particles as conditions are varied are summarized in Table 1. Also in Table 1 are the observed trends for GaN and AlN growth rates measured in our RDR [1,6], as well the general trends observed for In incorporation efficiency during InGaIn growth [27–29]. In all but one case, the scattering intensity is anticorrelated with the growth rate (or In incorporation efficiency), which is to be expected

Table 1
Trends for GaN and AlN near 1000°C, InN near 800°C

Action	GaN scattering intensity	GaN growth rate	AlN scattering intensity	AlN growth rate	InN scattering intensity	In incorporation efficiency
Temperature ↑	↑	↓	↑	↓	↑	↓
Total pressure ↑	↑↑	↓	↑↑	↓	↑↑	↑?
Residence time ↑	↑	↓	↑	↓	↑	?
Carrier gas switch H ₂ → N ₂	↓↓	↑	↑ Slightly	↓ Slightly	↓↓	↑↑

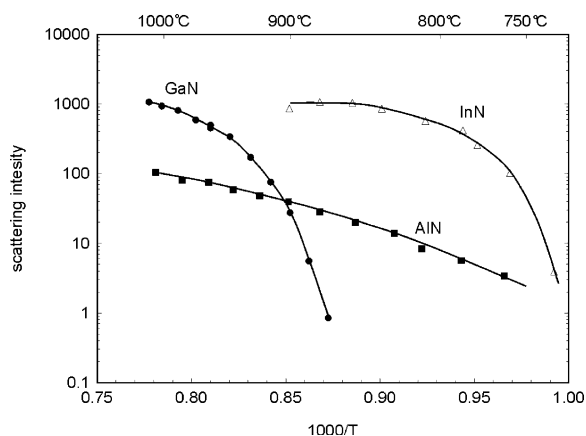


Fig. 3. Temperature dependence of the light scattering intensity for particles generated during GaN, AlN, and InN OMPVE, plotted in Arrhenius fashion. TMGa flow = 182 $\mu\text{mol/min}$, TMAI flow (monomer) = 68 $\mu\text{mol/min}$, TMIn flow = 59 $\mu\text{mol/min}$.

if the scattering intensity correlates with the magnitude of the parasitic chemical process. For InGaIn there are some reports of In incorporation increasing with total pressure [29], which does not correlate with the scattering intensity, and may be due to a competing In evaporation mechanism [30].

The temperature dependence of the nanoparticle scattering intensity for AlN, GaN, and InN is shown quantitatively in Fig. 3. The AlN and GaN measurements are over a wider temperature range than we previously reported [6], and curvature in the Arrhenius plots is now apparent. Note that GaN and AlN exhibit qualitatively different behavior. For AlN, nanoparticles are observable down to $\sim 750^\circ\text{C}$, and the intensity increases modestly with temperature. Due to the slight

curvature, the apparent activation energy ranges from 25–35 kcal/mol. Scattering for GaN conditions exhibits an extremely steep temperature dependence near 900°C , with the signal being below the detection limit at $T < 860^\circ\text{C}$. Between 950 – 1050°C the GaN signal exhibits an apparent activation energy of 60–70 kcal/mol.

The above trends are consistent with the growth rate temperature dependence observed in our RDR for similar OMVPE conditions. For GaN at 900°C the growth rate ($\Omega = 1200$ rpm) is at the transport limit, demonstrating that the parasitic chemistry is not affecting the growth rate at this temperature. As the temperature is raised further, the GaN growth rate begins to drop (by $\sim 25\%$ at 1050°C , $\Omega = 1200$ rpm), demonstrating the GaN parasitic chemistry becomes operative in the 900 – 1000°C range. For AlN, the growth rate at 900°C is substantially below the transport limit (less than half), demonstrating that the parasitic chemistry is already operative at this temperature. A similar temperature dependence was noted by Chen, et al. [2], who noted a drop in AlN growth rate above 600°C , and in GaN growth rate above 1000°C .

The particle scattering intensity for InN OMVPE (Fig. 3) is marked by a steep onset near 750°C . It is interesting to note that most InGaIn is deposited in the 700 – 800°C range. The In incorporation efficiency is strongly temperature dependent, and above 800°C very little indium incorporation occurs [27]. As we mentioned above, an alternative explanation for this observation is In desorption [30]. The scattering intensity for InN becomes nearly independent of temperature above 850°C . This may be a manifestation of nearly complete consumption of the In into particles, in which case the particles would stop growing and

the scattering intensity would become constant. Overall, the InN behavior looks similar to the GaN behavior, but with the onset shifted down in temperature by $\sim 150^\circ\text{C}$. If a radical mechanism, e.g. path-B in Fig. 1, is responsible for InN and GaN particle nucleation, then we would expect this temperature difference because TMIn pyrolysis occurs at a much lower temperature than TMGa pyrolysis [17–20].

Trends with temperature, total pressure, and residence time observed for GaN and AlN have the same direction (though the magnitudes may be different). However, the behavior when the carrier gas is switched from H_2 to N_2 is fundamentally different for GaN vs. AlN (see Table 1). In the case of GaN, switching to N_2 causes the scattering intensity to drop several orders of magnitude, often below the detection limit. In our RDR at the standard growth conditions (1200 rpm, 140 Torr, 1050°C), switching to N_2 causes the growth rate to increase to the transport limit, indicating the parasitic reaction mechanism is strongly quenched. For AlN, the opposite trend is observed: a slight increase in scattering intensity and a slight reduction of growth rate occurs upon replacing H_2 with N_2 . The carrier gas dependence of InN is similar to the GaN behavior; near 800°C , the scattering intensity drops orders-of-magnitude when H_2 is replaced with N_2 . This observation also correlates with the common use of N_2 carrier gas during InGaIn growth, and with the observation that small amounts of H_2 reduce the amount of In incorporation [28].

4. Infrared spectroscopy of $\text{M}(\text{CH}_3)_3 + \text{NH}_3$ mixtures (M = Al, Ga, In)

4.1. $\text{Al}(\text{CH}_3)_3 + \text{NH}_3$

The reaction of TMAI with NH_3 has been widely studied [31–33], and it is universally held that a classic Lewis acid-base complex (or adduct), $(\text{CH}_3)_3\text{Al}:\text{NH}_3$, is the first product formed. The IR spectrum of the gas-phase reaction product between TMAI and NH_3 at 99°C is shown in Fig. 4(a). The $\text{NH}_3(\text{g})$ absorption is removed by ratioing to a NH_3 reference spectrum, and the

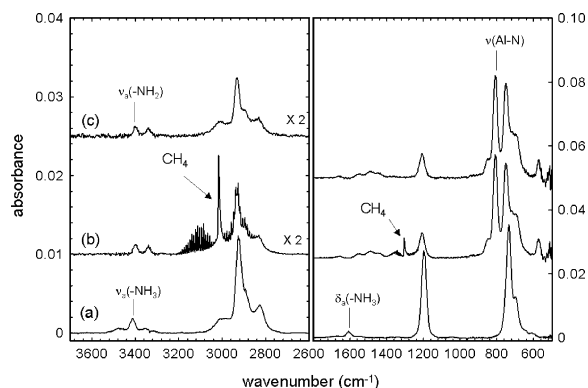


Fig. 4. IR spectra for a TMAI + NH_3 mixture at: (a) 99°C , (b) 268°C , (c) 268°C with CH_4 component subtracted. Conditions are; $P = 100$ Torr, TMAI flow = $59 \mu\text{mol}/\text{min}$, NH_3 flow = 1.0 slm , H_2 flow = 5.5 slm .

remaining peaks are indicative of both $-\text{NH}_3$ and $-\text{CH}_3$ vibrational modes. Although this is the first reported infrared spectrum for gas-phase TMAI: NH_3 , we can make the mode assignments based on earlier condensed phase spectra [31–33]. The asymmetric $-\text{NH}_3$ stretching mode, $\nu_a(\text{NH}_3)$, at 3412 cm^{-1} and the asymmetric $-\text{NH}_3$ bending mode, $\delta_a(\text{NH}_3)$, at 1609 cm^{-1} compare favorably with the matrix isolated TMAI: NH_3 values of 3396 and 1606 cm^{-1} , respectively [34]. At this temperature all of the remaining peaks can also be assigned to TMAI: NH_3 (a complete mode assignment will be reported elsewhere [21]). The peak near 1200 cm^{-1} is composed of the symmetric $-\text{CH}_3$ and $-\text{NH}_3$ deformation modes, i.e. $\delta_s(\text{CH}_3)$ and $\delta_s(\text{NH}_3)$. Due to the weakness of the Al–N donor–acceptor bond, the Al–N stretching mode is expected to be at $300\text{--}400 \text{ cm}^{-1}$ [34], which is below our detection limit.

Upon heating to $\sim 120^\circ\text{C}$ the production of CH_4 becomes detectable, and other changes begin to occur in the spectrum. Heating further to $\sim 250^\circ\text{C}$ drives this reaction to near completion. The spectrum for the mixture at 268°C is given in Fig. 4(b). Now characteristic CH_4 peaks at 3017 and 1305 cm^{-1} (as well as the rovibrational fine structure) are clearly evident. The CH_4 signal corresponds to a flow rate of $63 \pm 4 \mu\text{mol}/\text{min}$ (determined by comparing to CH_4 calibration experiments). This flow rate corresponds very

closely with one mole of CH_4 evolved per initial mole of TMAI (68 $\mu\text{mol}/\text{min}$) [35].

Subtracting the methane spectrum from curve Fig. 4(b) yields curve Fig. 4(c). The most noticeable new peak in this spectrum occurs at 809 cm^{-1} . Based on the experimental and theoretical work by Müller this peak can be assigned to the Al–N stretching mode, i.e. $\nu(\text{AlN})$, of the $(\text{CH}_3)_2\text{Al-NH}_2$ molecule [34]. This molecule now contains a strong covalent Al–N bond, which blue shifts the vibrational frequency into our detection range. The remaining peaks in Fig. 4(c) are also consistent with the $(\text{CH}_3)_2\text{Al-NH}_2$ molecule [34]. From the IR spectrum we cannot yet infer the degree of association (or lack thereof), but from volatility and thermodynamic arguments we believe we are seeing only the monomer. In any case, for the conditions at which this species is formed it is volatile and does not build up noticeable deposits on the cell wall or IR window.

4.2. $\text{Ga}(\text{CH}_3)_3 + \text{NH}_3$

The reactivity of TMGa with NH_3 has also been widely studied, and in this case there have been several reports of the gas-phase IR spectrum of the adduct, TMGa:NH_3 [36–38] in addition to the condensed phase spectrum reports [39]. The spectrum for TMGa:NH_3 , in Fig. 5(a) is in good agreement with the previous work. There are also similarities between the IR spectra of the Al

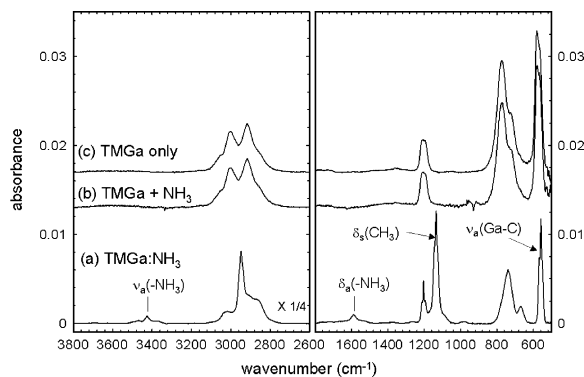


Fig. 5. IR spectra for a TMGa + NH_3 mixture at: (a) 53°C , (b) 269°C . (c) TMGa w/o NH_3 at 269°C . Conditions are; $P = 100$ Torr, TMGa flow = $182\text{ }\mu\text{mol}/\text{min}$, NH_3 flow = 1.0 slm , H_2 flow = 5.5 slm .

(Fig. 4a) and Ga (Fig. 5a) adducts; note the position and relative intensities of the $\nu_a(\text{NH}_3)$ and $\delta_a(\text{NH}_3)$ modes (3426 and 1588 cm^{-1} , respectively for TMGa:NH_3). However, for TMGa:NH_3 the $\delta_s(\text{CH}_3)$ mode (now at 1136 cm^{-1}) no longer overlaps with the $\delta_s(\text{NH}_3)$ mode near 1200 cm^{-1} . The $\delta_s(\text{CH}_3)$ mode for the adduct is also shifted significantly from the corresponding mode in pure TMGa, so it serves as a good indicator of the amount of adduct present. The TMGa adduct also exhibits a relatively strong asymmetric Ga–C stretching mode, $\nu_a(\text{Ga-C})$, at 559 cm^{-1} , whereas the corresponding mode for TMAI:NH_3 is very weak or absent.

Unlike the $\text{TMAI} + \text{NH}_3$ result, heating, the $\text{TMGa} + \text{NH}_3$ mixture to $\sim 200^\circ\text{C}$ does not produce a measurable amount of methane. Instead the $\text{TMGa} + \text{NH}_3 \leftrightarrow \text{TMGa:NH}_3$ equilibrium is simply shifted back towards the free TMGa side. The spectrum of a mixture at 269° is shown in Fig. 5(b). This curve is identical to the IR spectrum of TMGa in H_2 only, Fig. 5(c), taken at the same temperature and concentration. The $\delta_s(\text{CH}_3)$ mode of the adduct is completely absent. At intermediate temperatures the spectra (not shown) appear as a combination of TMGa:NH_3 and free TMGa. Raising the total pressure increases the TMGa and NH_3 concentration, and shifts the equilibrium to the right (more adduct). Further analysis should reveal the equilibrium constant for the $\text{TMGa} + \text{NH}_3$ reaction, but this is beyond the scope of this paper. The absence of a CH_4 -producing reaction up to $\sim 280^\circ\text{C}$ indicates that the reactivity of TMGa/NH_3 mixtures towards irreversible decomposition is not as facile as perhaps previously thought.

4.3. $\text{In}(\text{CH}_3)_3 + \text{NH}_3$

The reaction of TmIn with NH_3 has not been studied in as much detail as the corresponding TMAI or TMGa chemistry. Only one previous IR study has been reported [40], in this case for matrix-isolated (condensed-phase) TmIn:NH_3 . Our spectrum for the gas-phase adduct is shown in Fig. 6(a). Many qualitative similarities between the TmIn:NH_3 and TMGa:NH_3 adduct are apparent. However, the $-\text{NH}_3$ stretching and

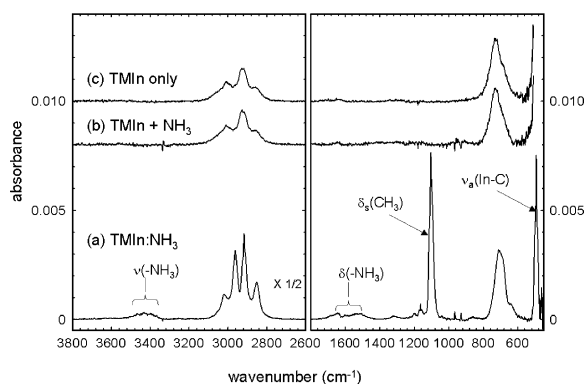


Fig. 6. IR spectra for a TMIn + NH₃ mixture at: (a) 23°C, (b) 269°C. (c) TMIn w/o NH₃ at 269°C. Conditions are; $P = 100$ Torr, TMIn flow = 59 $\mu\text{mol}/\text{min}$, NH₃ flow = 1.0 slm, H₂ flow = 5.5 slm.

deformation modes are broader and less distinct for TMIn:NH₃. The TMIn:NH₃ $\nu(\text{NH}_3)$ mode is centered at 3430 cm^{-1} , which is very close to the TMGa:NH₃ $\nu_a(\text{NH}_3)$ peak at 3426 cm^{-1} . Piocos and Ault [40] did not report results above 2000 cm^{-1} so we cannot make a comparison. The $\delta(\text{NH}_3)$ mode position(s) are harder to ascertain, in part because of interference from residual NH₃(g) absorption at 1626 cm^{-1} . Our tentative assignment puts the $\delta_a(\text{NH}_3)$ mode at 1642 cm^{-1} , which is in reasonable agreement with the value of 1665 cm^{-1} reported by Pioco and Ault [40]. Based on similarities with the TMGa:NH₃, we assign the intense peak at 1106 cm^{-1} seen for TMIn:NH₃ to the $\delta_s(\text{CH}_3)$ mode. The TMIn adduct also exhibits a relatively strong asymmetric In–C stretching mode, $\nu_a(\text{In–C})$, at 494 cm^{-1} , which is 65 cm^{-1} lower than the corresponding mode for TMGa:NH₃.

As the TMIn + NH₃ mixture is heated to $\sim 200^\circ\text{C}$ simple adduct dissociation occurs, analogous to the case for TMGa:NH₃. The spectrum of a mixture at 269°C is shown in Fig. 6(b). No CH₄ peaks are detected, and the spectrum is identical to TMIn in H₂, Fig. 6(c). Spectra in the $100\text{--}200^\circ\text{C}$ range appear as combinations of TMIn:NH₃ and TMIn. The behavior is qualitatively very similar to the TMGa:NH₃ results, and our preliminary analysis even demonstrates that the equilibrium constants for the two adducts are of the same order-of-magnitude.

Heating TMIn + NH₃ mixtures further to 300°C resulted in a small amount of CH₄ formation. However, removing NH₃ did not reduce the amount of CH₄ formed, so it is likely that these conditions simply represent the beginning of homogeneous and/or heterogeneous TMIn decomposition in H₂. In fact, our CH₄ production rate is consistent with literature values for TMIn decomposition [20]. Experiments using N₂ as the carrier gas (with or w/o NH₃) produced no measurable CH₄ production at otherwise identical conditions. The N₂ experiments imply that H₂ is somehow enhancing TMIn decomposition, which has been noted in previous work [20].

5. Conclusions

Light scattering experiments in an inverted stagnation point flow reactor have produced direct observation of particle formation during AlGaInN OMVPE. The particles are formed by chemical reactions that require the high temperatures encountered in the boundary layer. Thermophoresis keeps the particles from reaching the surface so they do not contribute to the deposition rate. A simple CVD based particle-growth mechanism can explain particle sizes in the observed range. This mechanism also predicts a strong residence time dependence. A mechanism with a strong τ dependence is required to explain the strong spin rate dependence we previously observed for OMVPE growth rates in our RDR [6].

All qualitative trends of the scattering intensity for AlN and GaN are anticorrelated with growth rate trends, which is to be expected if the scattering signal is a measure of the degree of a parasitic process. Both GaN and InN scattering exhibit sharp thresholds with respect to temperature, while AlN exhibits a much weaker temperature dependence. Both GaN and InN scattering are strongly quenched when the carrier gas is switched from H₂ to N₂, in contrast to the AlN behavior.

The FTIR results also show a difference between the AlN vs. GaN (or InN) behavior. All three precursors form the expected (CH₃)₃M:NH₃ species, but only TMAI exhibits a facile CH₄ elimination reaction for the conditions studied.

Both TMGa:NH₃ and TMIn:NH₃ exhibit reversible adduct formation up to ~280°C, with no measurable CH₄ production. This observation agrees with recent theoretical work by Sengupta [41], who demonstrated that the TMGa:NH₃ methane elimination reaction produces negligible amounts of (CH₃)₂GaNH₂ over a wide temperature range. Much higher concentrations of TMGa and NH₃, as used by Thon and Kuech [42], could maintain an appreciable adduct concentration to higher temperatures and possibly open up the CH₄ production channel.

Based on the results from nanoparticle and FTIR experiments, we conclude that the AlN particle-nucleation mechanism is predominately of a concerted nature, i.e. Fig. 1(a), while the GaN and InN particle-nucleation mechanisms involve radical chemistry, i.e. Fig. 1(b). Using a theoretical analysis, Talalaev et al. reached a similar conclusion for InN chemistry [43]. Many details of each mechanism remain to be uncovered, but the global features of the parasitic chemical pathways for AlN, GaN, and InN have been identified.

Acknowledgements

The authors thank R.P. Pawlowski for the 2D MPSalsa simulation of the inverted stagnation point reactor. The authors also thank D. Koleske for a critical reading of this manuscript, and T.M. Kerley, M.J. Russell, and L. Bruska for technical assistance. This research was performed at Sandia National Laboratories, for the United States Department of Energy under contract No. DE-AC04-94AL85000. We especially acknowledge support from the Office of Basic Energy Sciences.

References

- [1] J. Han, J.J. Figiel, M.H. Crawford, M.A. Banas, M.E. Bartram, R.M. Biefeld, Y.K. Song, A.V. Nurmikko, *J. Crystal Growth* 195 (1998) 291.
- [2] C.H. Chen, H. Liu, D. Steigerwald, W. Imler, C.P. Kuo, M.G. Craford, M. Ludowise, S. Lester, J. Amano, *J. Electron. Mater.* 25 (1996) 1004.
- [3] K. Sayyah, B.-C. Chung, M. Gershenzon, *J. Crystal Growth* 77 (1986) 424.
- [4] F. Nakamura, S. Hashimoto, M. Hara, S. Imanaga, M. Ikeda, H. Kawai, *J. Crystal Growth* 195 (1998) 280.
- [5] S.A. Safvi, J.M. Redwing, M.A. Tischler, T.F. Kuech, *J. Electrochem. Soc.* 144 (1997) 1789.
- [6] J.R. Creighton, M.E. Coltrin, W.G. Breiland, *ECS Proceedings, Vols. 2002–2003*, pp. 28–35.
- [7] J.R. Creighton, W.G. Breiland, M.E. Coltrin, R.P. Pawlowski, *Appl. Phys. Lett.* 81 (2002) 2626.
- [8] F.C. Sauls, L.V. Interrante, Z. Jiang, *Inorg. Chem.* 29 (1990) 2989.
- [9] L.V. Interrante, G.A. Sigel, M. Garbaskas, C. Hejna, G.A. Slack, *Inorg. Chem.* 28 (1989) 252.
- [10] M.J. Almond, M.G.B. Drew, C.E. Jenkins, D.A. Rice, *J. Chem. Soc. Dalton Trans.* (1992) 5.
- [11] C.C. Amato, J.B. Hudson, L.V. Interrante, *Appl. Surf. Sci.* 54 (1992) 18.
- [12] T.G. Mihopoulos, V. Gupta, K.F. Jensen, *J. Crystal Growth* 195 (1998) 733.
- [13] O. Makino, K. Nakamura, A. Tachibana, H. Tokunaga, N. Akutsu, K. Matsumoto, *Appl. Surf. Sci.* 159–160 (2000) 374.
- [14] R.M. Watwe, J.A. Dumesic, T.F. Kuech, *J. Crystal Growth* 221 (2000) 751.
- [15] A.Y. Timoshkin, H.F. Bettinger, H.F. Schaefer III, *J. Phys. Chem.* 105 (2001) 3240.
- [16] J.R. Creighton, *J. Electron. Mater.* 31 (2002) 1337.
- [17] M.G. Jacko, S.J.W. Price, *Can. J. Chem.* 41 (1964) 1560.
- [18] M.D. Allendorf, C.F. Melius, C.W. Baushlicher Jr., *J. Phys. IV France* 9 (1999) 23.
- [19] C.A. Larsen, N.I. Buchan, G.B. Stringfellow, *J. Crystal Growth* 102 (1990) 103.
- [20] A.H. McDaniel, M.D. Allendorf, *Chem. Mater.* 12 (2000) 450.
- [21] J.R. Creighton, manuscript in preparation.
- [22] A.G. Salinger, K.D. Devine, G.L. Hennigan, H.K. Moffat, S.A. Huthcinson, J.N. Shadid, Sandia National Laboratories, Report SAND96-2311/1996.
- [23] D.J. Ehrlich, J.Y. Tsao, *J. Vac. Sci. Technol. B* 1 (1983) 969.
- [24] R.A. Dobbins, C.M. Megaridis, *Langmuir* 3 (1987) 254.
- [25] J.R. Creighton, unpublished results.
- [26] W.G. Breiland, G.H. Evans, *J. Electrochem. Soc.* 138 (1991) 1806.
- [27] S. Keller, B.P. Keller, D. Kapolnek, A.C. Abare, H. Masui, L.A. Coldren, U.K. Mishra, S.P. DenBaars, *Appl. Phys. Lett.* 68 (1996) 3147.
- [28] E.L. Piner, M.K. Behbehani, N.A. El-Masry, F.G. McIntosh, J.C. Roberts, K.S. Boutros, S.M. Bedair, *Appl. Phys. Lett.* 70 (1997) 461.
- [29] A.D. Hanser, A.D. Banks, R.F. Davis, B. Jahn, M. Albrecht, W. Dorsch, S. Christiansen, H.P. Strunk, *Mater. Sci. Semicond. Proc.* 3 (2000) 163.
- [30] T. Matsuoka, N. Yoshimoto, T. Sasaki, A. Katsui, *J. Electron. Mater.* 21 (1992) 157.
- [31] F. Watari, S. Shimizu, K. Aida, E. Takayama, *Bull. Chem. Soc. Japan* 51 (1978) 1602.
- [32] B.S. Ault, *J. Phys. Chem.* 96 (1992) 7908.

- [33] J. Müller, U. Ruschewitz, O. Indris, H. Hartwig, W. Stahl, *J. Am. Chem. Soc.* 121 (1999) 4647.
- [34] J. Müller, *J. Am. Chem. Soc.* 118 (1996) 6370.
- [35] TMAI flows were calculated using the vapor pressure expression from G. B. Stringfellow, *Organometallic Vapor-Phase Epitaxy*, 2nd Edition, Academic Press, San Diego, CA, 1999, Table 4.5.
- [36] B.S. Sywe, J.R. Schlup, J.H. Edgar, *Chem. Mater.* 3 (1991) 737.
- [37] M.J. Almond, C.E. Jenkins, D.A. Rice, K. Hagen, *J. Organomet. Chem.* 439 (1992) 251.
- [38] S.H. Kim, H.S. Kim, J.S. Hwang, J.G. Choi, P.J. Chong, *Chem. Mater.* 6 (1994) 278.
- [39] J.R. Durig, C.B. Bradley, J.D. Odom, *Inorg. Chem.* 21 (1982) 1466.
- [40] E.A. Piocos, B.S. Ault, *J. Mol. Struct.* 476 (1999) 283.
- [41] D. Sengupta, *J. Phys. Chem. B* 107 (2003) 291.
- [42] A. Thon, T.F. Kuech, *Appl. Phys. Lett.* 69 (1996) 55.
- [43] R.A. Talalaev, E.V. Yakovlev, S.Y. Karpov, I.Y. Evstratov, A.N. Vorobev, Y.N. Makarov, *Phys. Stat. Sol. A* 176 (1999) 253.